



This is a repository copy of *Achieving high quality factor interband nanoplasmonics in the deep ultraviolet spectrum via mode hybridization*.

White Rose Research Online URL for this paper:

<https://eprints.whiterose.ac.uk/223333/>

Version: Accepted Version

Article:

Csányi, E., Liu, Y. orcid.org/0000-0003-4969-1888, Kai, D. orcid.org/0000-0002-2330-3480 et al. (10 more authors) (2025) Achieving high quality factor interband nanoplasmonics in the deep ultraviolet spectrum via mode hybridization. *Nano Letters*, 25 (10). pp. 3906-3913. ISSN 1530-6984

<https://doi.org/10.1021/acs.nanolett.4c06247>

© 2025 The Authors. Except as otherwise noted, this author-accepted version of a journal article published in *Nano Letters* is made available via the University of Sheffield Research Publications and Copyright Policy under the terms of the Creative Commons Attribution 4.0 International License (CC-BY 4.0), which permits unrestricted use, distribution and reproduction in any medium, provided the original work is properly cited. To view a copy of this licence, visit <http://creativecommons.org/licenses/by/4.0/>

Reuse

This article is distributed under the terms of the Creative Commons Attribution (CC BY) licence. This licence allows you to distribute, remix, tweak, and build upon the work, even commercially, as long as you credit the authors for the original work. More information and the full terms of the licence here:

<https://creativecommons.org/licenses/>

Takedown

If you consider content in White Rose Research Online to be in breach of UK law, please notify us by emailing eprints@whiterose.ac.uk including the URL of the record and the reason for the withdrawal request.



eprints@whiterose.ac.uk
<https://eprints.whiterose.ac.uk/>

Achieving High Quality Factor Interband Nanoplasmonics in the Deep Ultraviolet Spectrum via Mode Hybridization

Evelin Csányi^{1,2,†}, Yan Liu^{1,3,†}, Dan Kai^{1,4}, Sigit Sugiarto⁴, Henry Yit Loong Lee^{1,4}, Febiana Tjiptoharsono¹, Qifeng Ruan⁵, Soroosh Daqiqeh Rezaei⁵, Xiao Chi^{6,7}, Andriwo Rusydi^{6,7}, Graham Leggett², Joel K. W. Yang^{5,*} and Zhaogang Dong^{1,3,5,*}

¹Institute of Materials Research and Engineering (IMRE), Agency for Science, Technology and Research (A*STAR), 2 Fusionopolis Way, Innovis #08-03, Singapore 138634, Republic of Singapore

²Department of Chemistry, University of Sheffield, Brook Hill, Sheffield S3 7HF, United Kingdom

³Quantum Innovation Centre (Q.InC), Agency for Science Technology and Research (A*STAR), 2 Fusionopolis Way, Innovis #08-03, Singapore 138634, Republic of Singapore

⁴Institute of Sustainability for Chemicals, Energy and Environment (ISCE²), Agency for Science, Technology and Research (A*STAR), 1 Pesek Road, 627833, Singapore

⁵Singapore University of Technology and Design, 8 Somapah Road, 487372, Singapore

⁶Singapore Synchrotron Light Source (SSLS), National University of Singapore, 5 Research Link, 117603, Singapore

⁷Department of Physics, 2 Science Drive 3, National University of Singapore, 117542, Singapore

[†]These authors equally contribute to this work.

*Correspondence and requests for materials should be addressed to Z.D. (email: zhaogang_dong@sutd.edu.sg), and J.Y. (email: joel_yang@sutd.edu.sg).

ABSTRACT

Interband plasmons (IBPs) enable plasmonic behavior in non-metallic materials, such as semiconductors. Originating from interband electronic transitions, IBPs are characterized by negative real permittivity that can extend into deep ultraviolet (DUV) spectrum, as demonstrated using silicon. However, the practical applications of IBPs are limited by their inherently broad resonances. In this study, we address this limitation by hybridizing the localized plasmon resonance of silicon nanostructures with the Fabry-Pérot resonance of SiO₂ dielectric layer atop silicon substrate. This design achieves a simulated quality factor (Q -factor) of ~ 43 , with experimental measurements yielding a Q -factor of 37 at ~ 4.6 eV within the DUV region. Furthermore, we demonstrate a 5.4-fold enhancement in DUV absorption for lignin-modified polyethylene glycol films when integrated with the hybridized DUV cavity, showcasing the potential for UV blocking applications. Our findings offer a versatile platform that can be adapted to other IBP systems, and open new opportunities in UV-specific applications.

KEYWORDS: UV plasmonics; Interband plasmonics (IBP); *c*-Si nanodisk; *c*-Si nanohole; Localized surface plasmon resonance (LSPR); Optical mode hybridization.

Introduction

Interband plasmonics (IBPs), supported by non-metals, semiconductors and topological insulators, have attracted fast-growing interest in recent years.¹⁻³ Unlike classical plasmonic materials, such as gold (Au) and silver (Ag), where the plasmonic nature originates from the interaction between light and free electrons in the metal, IBPs rely on the electron interband transitions within the material. As a result, *p*-block IBP materials, such as silicon (Si), bismuth (Bi), gallium (Ga) and arsenic (As), exhibit a strong plasmonic character in the ultraviolet (UV) and visible spectral range, while antimony (Sb) displays this behavior in the visible to near-infrared region.^{1, 2} These characteristics extend to their dichalcogenides and binary compounds, including antimony triselenide (Sb₂Se₃), antimony telluride (Sb₂Te₃),⁴ bismuth triselenide (Bi₂Te₃) and bismuth telluride (Bi₂Te₃).^{5, 6} Owing to their unique optical, physical and chemical properties, the application of these compounds can offer advantages over conventional plasmonic materials, and are currently being explored as materials for surface-enhanced spectroscopy,⁷⁻⁹ thermoelectrics,^{10, 11} tuneable plasmonics,¹²⁻¹⁴ and ultra-wide band detectors.^{4, 15}

Despite their outstanding potential, leveraging the plasmonic nature of IBP materials has been challenging due to their intrinsically large damping losses (*i.e.*, extinction coefficient, k), which consequently leads to plasmonic resonances with low quality factors (Q -factors).² For example, Si nanodisk structures can support localized surface plasmon resonances (LSPR) with strong optical field enhancements in sub-10-nm gaps in the UV spectrum.¹⁶ However, the Q -factor of the resonances is typically ~ 1 . Generally, the quality factor of currently known IBP materials does not exceed 3.² This problem severely limits their applications in optical sensors,¹⁷ photodetectors^{18, 19} and other optoelectronic devices, which require high sensitivity with the sharp and sensitive resonances.²⁰⁻²³ To fully utilise the extraordinary plasmonic

properties of IBP materials, the Q -factor of the resonances could therefore be enhanced by exploring nanoantenna designs.²⁴⁻²⁷

In this work, we hybridize the localized plasmon resonance of silicon nanodisk arrays with the Fabry-Pérot (F - P) resonance of a SiO₂ dielectric layer on top of a silicon substrate, achieving a simulated Q -factor of ~ 43 . The experimental measured Q -factor is 37 with a narrow line width of ~ 7 nm within the deep UV region at ~ 4.6 eV. The observed Q -factors are higher than that reported for UV plasmonic Al nanodisks of a similar design.²¹ In particular, the use of Si over Al offers additional advantages in terms of stability and easier integration with existing semiconductor fabrication methods. The enhanced sensitivity and light absorption of the high- Q resonance is demonstrated by depositing a UV-absorbing lignin-polyethylene glycol (lignin-PEG) co-polymer film over the plasmonic array. Lignin-PEG exhibits a strong absorption at ~ 4.54 eV, falling within the spectral range of the IBP resonances demonstrated in our work, thus facilitating effective interaction between these two materials. Our results indicate that optical mode hybridization leads to exceptionally high-quality resonances for IBP materials, therefore drastically improving the outlook for applications where narrow resonances are required. Moreover, Si nanodisk arrays of this nature can potentially be utilized in UVC (100-280 nm) specific applications, such as investigations of germicidal mechanisms,^{28, 29} enhancement of light-absorption,^{30, 31} UV sensors and photodetectors.³²⁻³⁵

Results and discussion

The interband plasmonic properties of crystalline silicon (c -Si) nanodisk arrays were studied by examining hybridized optical resonance modes in the deep ultraviolet (DUV) region. The arrays were fabricated on a Si substrate with a 300-nm SiO₂ dielectric spacer layer (see *Methods*), as shown in Figure 1(a). The bottom Si substrate acts as a reflector, enabling hybridization between the LSPR mode on the nanodisks and the F - P cavity mode. The

hybridized state's sharpness and resonance band linewidth are influenced by the degree of hybridization. This interaction can be precisely controlled by adjusting two parameters: the SiO₂ spacer layer thickness and the nanodisk diameter.

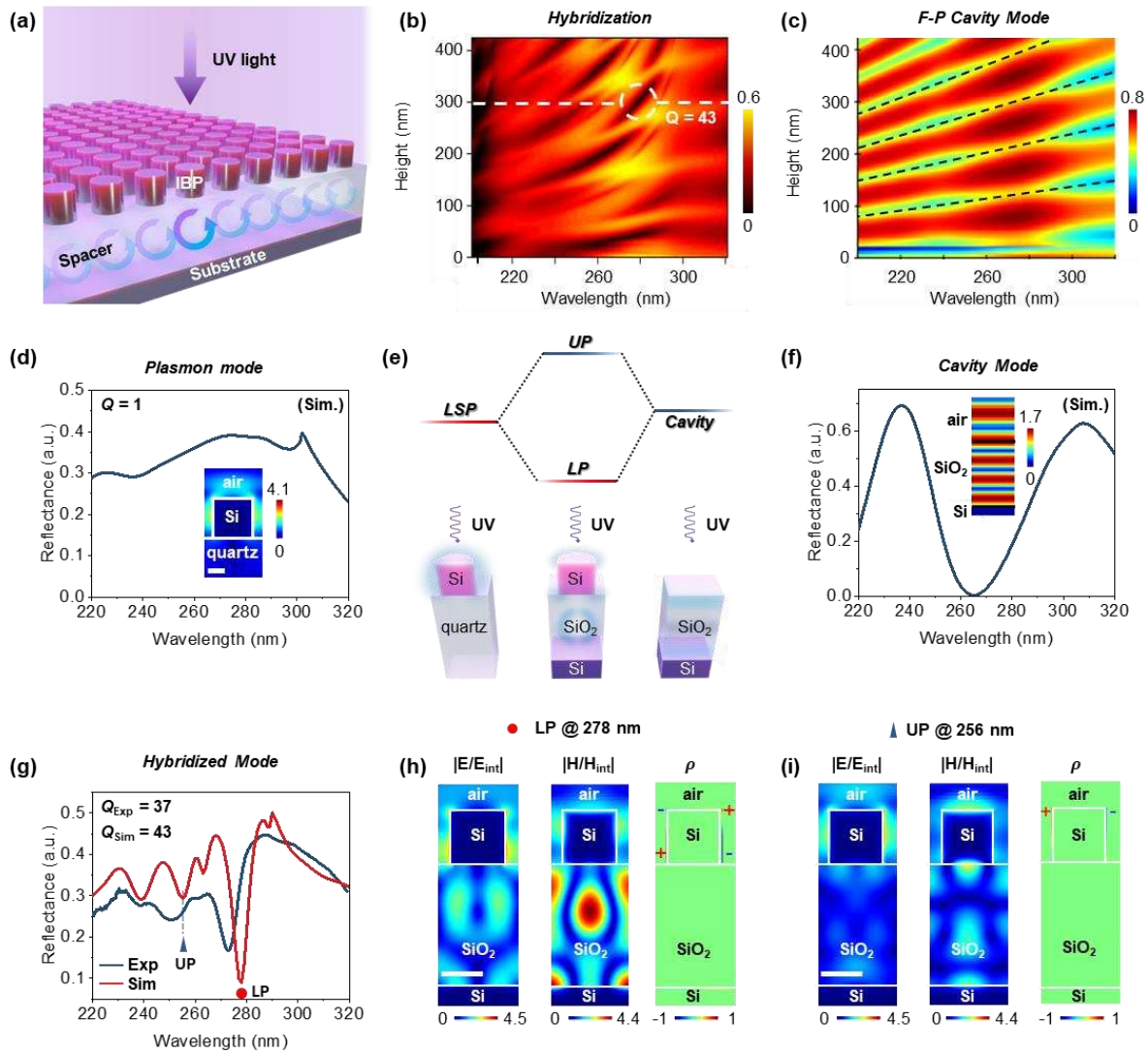


Figure 1. High- Q resonances of the Si interband plasmonic nanodisk array achieved via mode hybridization at DUV wavelengths. (a) Schematic of the array of interband plasmonic (IBP) nanodisks fabricated on top of SiO₂/Si substrate. (b) Simulated reflectance spectra for c -Si nanodisk arrays on the SiO₂/Si substrate, showing the degree of hybridization between the LSPR mode of the c -Si nanodisks and the F - P cavity resonance mode. The simulated reflectance spectrum has a Q -factor of 43. (c) Reflectance spectra of the F - P cavity as a

function of the cavity (SiO_2) height. (d) Simulated reflectance spectrum of the *c-Si* nanodisk array ($h_{\text{Si}} = 130 \text{ nm}$, $d = 130 \text{ nm}$, $p = 200 \text{ nm}$) on a quartz substrate, exhibiting a Q -factor of 1. (e) Schematic illustration of the hybridization mechanism between LSP and F - P cavity resonances. (f) Simulated reflectance spectrum of the F - P cavity with a film of 15 nm Ag on 300 nm SiO_2/Si substrate, showing a Q -factor of 7. (g) Theoretical and experimentally measured reflectance spectrum of the LP mode of *c-Si* nanodisk/300 nm SiO_2/Si ($h_{\text{Si}} = 130 \text{ nm}$, $d = 130 \text{ nm}$, $p = 200 \text{ nm}$). (h)-(i) Spatial distribution of the electric field $|E/E_{\text{int}}|$, magnetic field $|H/H_{\text{int}}|$, and charges within the cross-section of *c-Si* nanodisks on 300 nm SiO_2/Si , demonstrating the LP mode and UP mode. The scale bar denotes 100 nm.

The thickness of the SiO_2 spacer layer significantly influences the system's optical response via hybridization. We analyzed this using finite-domain time-difference (FDTD) simulation. Figure 1(b) shows the simulated reflectance spectra as a function of F - P cavity thickness, with the *c-Si* antenna array having a height of 130 nm, disk diameter of 130 nm, and pitch of 200 nm. Simulation details are in *Numerical Simulations*, while reflectance spectra and electrical field mode distributions for F - P cavity thicknesses of 100 nm, 200 nm, and 300 nm are in Figure S1. The optimized 300 nm F - P cavity achieves the highest Q -factor of 43. The polycrystalline silicon (*c-Si*) nanoarray was fabricated with an annealing process after nanopatterning (see *Methods*). This conversion to crystalline silicon improves the Q -factor, as shown in Figure S2, where it was obtained via Gaussian fitting (Figure S3). This improvement is due to *c-Si*'s lower optical losses compared to amorphous silicon, stemming from reduced structural disorder and absence of mid-gap defect states.³⁶

For the *c-Si* nanodisk array ($d = 130 \text{ nm}$) on a quartz substrate (without the spacer cavity), interband plasmonics exhibit a broad resonance ($Q = 1$) (Figure 1(d)), attributed to *c-Si*'s lossy nature and significant UV absorption. However, mode hybridization between the

c-Si IBP nanodisk and the *F*-*P* cavity (Figure 1(e)) alters the optical response, modifying the behaviors of both nanodisk LSPR and *F*-*P* cavity (Figures 1(f) and S5). This hybridization generates high-*Q* resonances and, in periodic nano hole-patterned systems, enables nonlocal resonances with high *Q*-factors.^{37, 38} The process produces two hybrid modes: the upper polariton (UP) and lower polariton (LP) modes, shown in 3D plots in Figure S6.

Both hybrid modes appear in the experimental reflectance spectrum in Figure 1(g). The sharper LP mode at $\lambda = 278$ nm (red dot) has a theoretical *Q*-factor of 43 and a measured *Q*-factor of 37, with corresponding electric field, magnetic field, and charge distributions illustrated in Figure 1(h). The LP mode enhances scattering at the nanodisk corners, behaving like a quadrupole in the charge distribution. Conversely, the broader UP mode at $\lambda = 256$ nm (blue triangle) exhibits higher radiative loss due to its dipolar nature, as reflected in the charge distribution (Figure 1(i)).

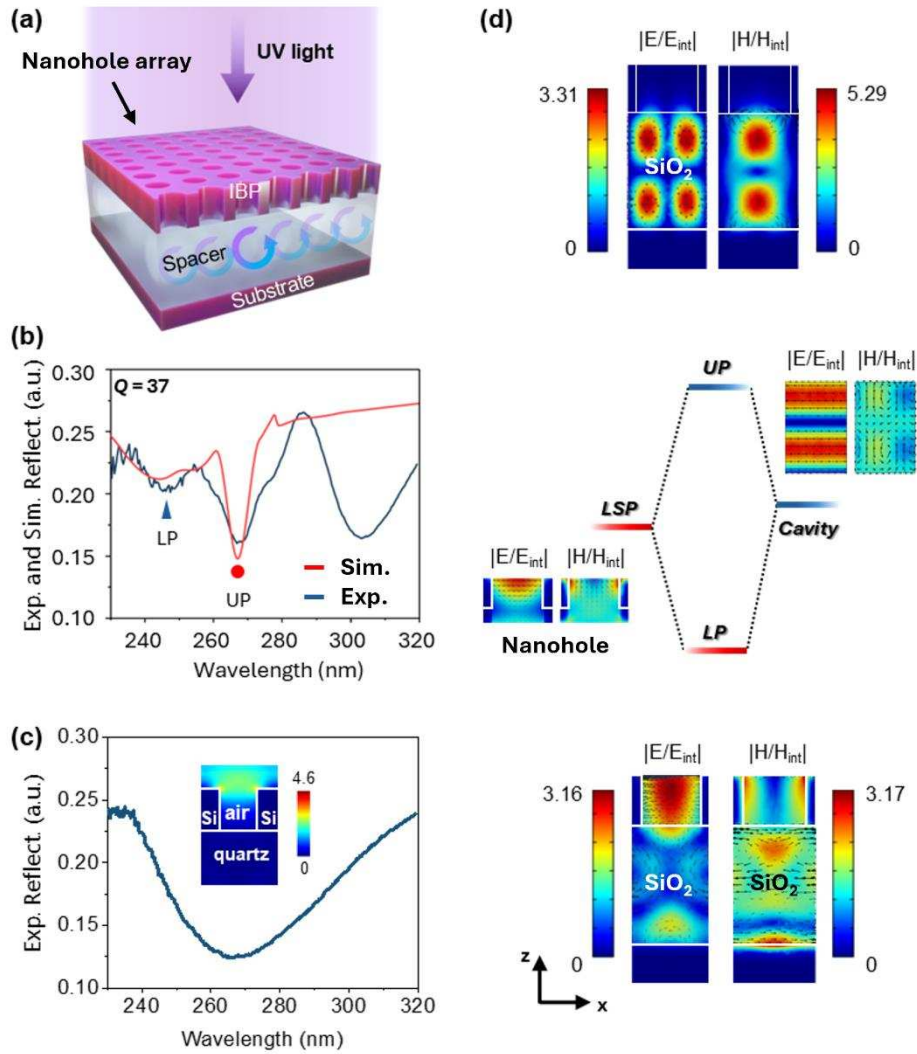


Figure 2. Mode hybridization of the Si nanohole plasmons with the F - P cavity. (a) Schematic illustration of the hybrid plasmonic cavity of the Si interband plasmonic (IBP) nanoholes on a F - P cavity. (b) Experimentally measured reflectance spectrum of a hybrid mode in nanoholes ($h_{Si} = 130$ nm, $d = 150$ nm, $p = 200$ nm), with a corresponding Q -factor of 37. The red line presents the simulated reflectance spectrum. (c) Experimental reflectance of the c -Si nanohole array ($h_{Si} = 130$ nm, $d = 150$ nm, $p = 200$ nm) on quartz substrate (without F - P cavity), with a Q -factor of 5. (d) Energy level diagram of the hybridization, showing the LSPR mode in c -Si nanohole and F - P cavity resonance mode in the SiO_2 spacer. Simulated spatial distribution of the electric field $|E/E_{int}|$ and magnetic field $|H/H_{int}|$ in the hybrid UP/LP mode

illustrates a stronger interaction between LSPR and F - P cavity in LP mode than that in UP mode.

LSPR void modes also exist in c - Si nanoholes.¹⁶ Figure 2(a) shows a c - Si nanohole array ($h_{Si} = 130$ nm, $d = 150$ nm, $p = 200$ nm) atop a dielectric SiO_2 layer on a Si substrate, with measured and simulated reflectance spectra in Figure 2(b). Hybridization of LSPR and F - P cavity modes generates two optical modes: the UP mode (blue triangle) and LP mode (red dot). The LP mode creates a resonance dip at $\lambda = 270$ nm with a narrow linewidth, achieving a Q -factor of 37 (Figure 2(b)), close to the theoretical Q -factor of 39. By contrast, a c - Si nanohole array with identical geometry on a quartz substrate without the cavity film shows a broad resonance at $\lambda = 270$ nm, with a Q -factor of 5 (Figure 2(c)).

To explore the nature of the two hybrid modes in c - Si nanoholes on the SiO_2/Si cavity, eigenstate calculations were performed using finite-element analysis. The LSPR and F - P cavity modes were calculated separately, as shown in the energy level diagram in Figure 2(d), with the hybridized modes labeled LP and UP. Simulations reveal stronger electric-field enhancement in the nanohole structure at the LP mode than at the UP mode.

To control the degree of hybridization, we tuned mode hybridization characteristics by adjusting geometrical parameters for nanodisk and nanohole arrays on 300-nm SiO_2/Si , as shown in Figure 3(a)-(b). Fixing the array pitch at 200 nm yielded the sharpest reflectance resonances (Figure S7). Simulated angle-resolved reflectance of nanodisk arrays reveals that increasing the SiO_2 spacer thickness enhances the resonance Q -factor and causes a redshift (Figure S8).

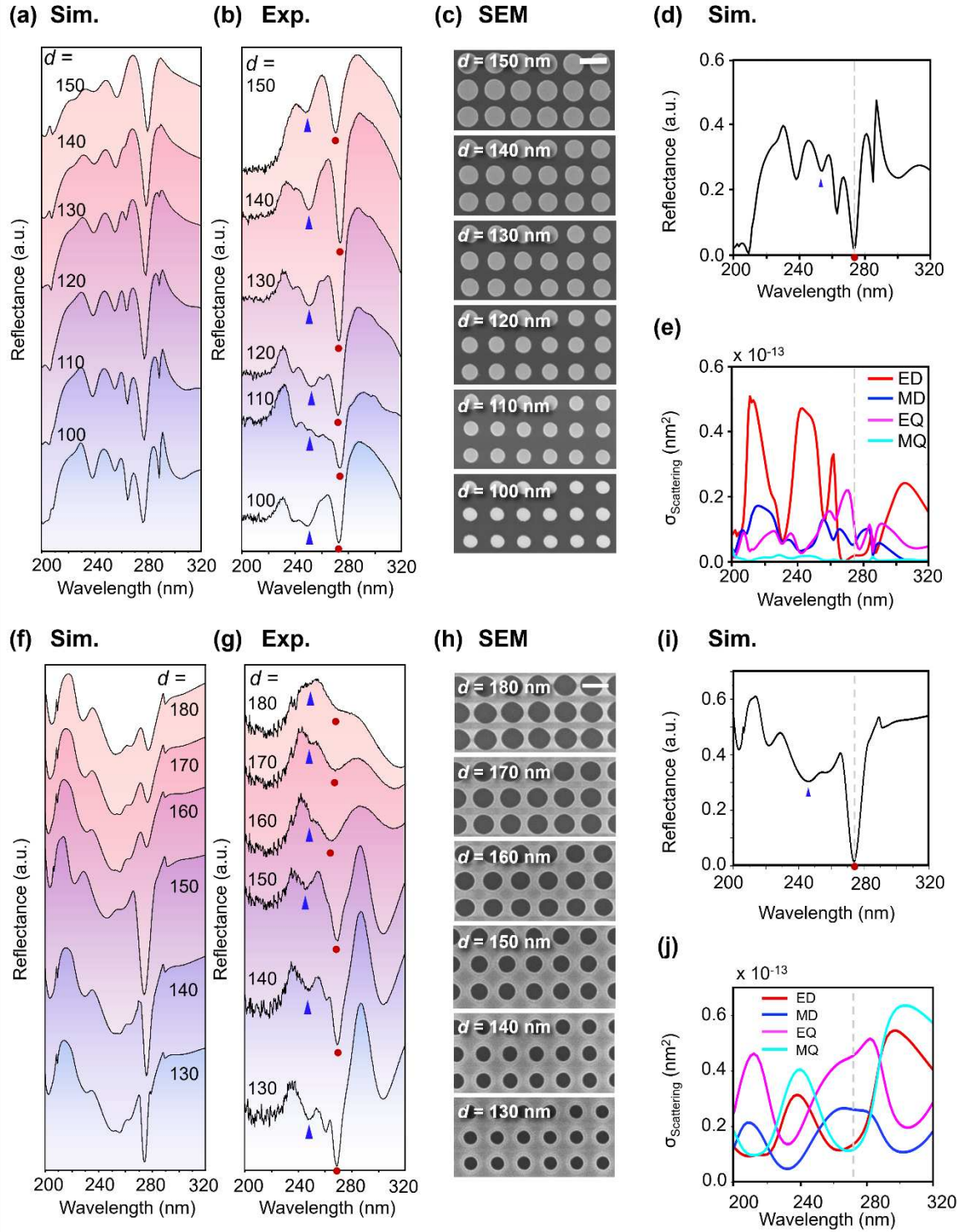


Figure 3. Engineering of the mode hybridization characteristics via geometrical parameter tuning. (a) Simulated and (b) experimental reflectance of the *c*-Si nanodisk arrays of varying diameter from 100 nm to 150 nm, and fixed $p = 200$ nm, $h_{Si} = 130$ nm, $h_{SiO_2} = 300$ nm. (c) Corresponding SEM images of the same arrays (scale bar denotes 100 nm). (d) Simulated reflectance spectrum of a nanodisk array ($Q = 43$, with $p = 200$ nm, $h_{Si} = 130$ nm,

$h_{SiO_2} = 300$ nm and $d = 130$ nm), and (e) the corresponding multipolar decomposition of the scattering cross section ($\sigma_{scattering}$). (f) Simulated and (g) experimental reflectance of the *c-Si* nanohole arrays, with hole diameters ranging from 130 nm to 180 nm of varying diameter, and $p = 200$ nm, $h_{Si} = 130$ nm, $h_{SiO_2} = 300$ nm. (h) Corresponding SEM images (the scale bar denotes 100 nm). (i)-(j) Simulated reflectance spectrum of the nanohole array ($p = 200$ nm, $h_{Si} = 130$ nm, $h_{SiO_2} = 300$ nm and $d = 150$ nm), and corresponding multipolar decomposition, respectively.

The LP mode resonance dips (red dots) of the arrays remain at ~ 278 nm, largely unaffected by changes in nanodisk dimensions, while the UP modes (blue triangles) are located at ~ 256 nm. Both hybridized resonances show minimal spectral shifts due to the broad nature of the nanodisk's localized plasmon resonance. Although slight redshifts occur with increasing diameter, the reflectance spectrum remains largely unchanged, reducing sensitivity to size variations. However, diameter adjustments affect the sharpness of the resonance dip. Figure 3(d) shows the simulated reflectance spectrum of the nanodisk array, with a theoretical Q -factor of 43 for the LP mode. Multipolar decomposition of the scattering cross-section indicates a dominant electric quadrupole (EQ) near the resonance dip (Figure 3(e)). Eigenmode analysis reveals the resonance interaction arises from coupling between the EQ on the *c-Si* nanodisk and a vertical $F-P$ cavity mode, as shown in Figures S6.

Similar behavior was observed in Si nanohole arrays. Figures 3(f)-3(g) show the simulated and experimental reflectance spectra, while SEM images in Figure 3(h) depict arrays with hole diameters ranging from 130 nm to 180 nm. Resonance dips are located at $\lambda = 278$ nm (Figure 3(i)). The theoretical Q -factor of the LP mode (red dots) rises to 39 as the hole diameter increases from 130 nm to 150 nm but decreases beyond this point. The narrow spectral resonance linewidth originates from the hybridization of the electric quadrupole plasmonic

mode with the F - P cavity mode, as verified by multipolar analysis (Figure 3(j)). In summary, the Q -factor and DUV power absorption of hybrid IBP nanodisk and nanohole arrays can be enhanced by engineering disk and hole dimensions, with related UV absorption simulations in Figure S9.

To highlight the advantages of high- Q -factor c -Si IBP arrays, we examined their impact on enhancing UV absorption in a thin layer of UV-absorbing material. Figure 4(a) illustrates the role of IBP arrays in boosting UV absorption in lignin-PEG polymer films (see Figure S10). The modified lignin copolymer, lignin-PEG (Figure 4(b)), was synthesized following the method by P. Y. M. Yew et al.³⁹ Due to its aromatic ring network, lignin exhibits strong absorption at ~ 273 nm, aligning with the plasmon dip of Si arrays with $d = 130$ nm, $p = 200$ nm, and $h_{SiO_2} = 300$ nm. Nanodisk arrays were spin-coated with lignin-PEG at varying rpm to achieve conformal polymer films of different thicknesses. Film thickness was measured using spectroscopic ellipsometry on the substrate's flat region, and the refractive index (n) and extinction coefficient (k) were extracted from spectral fitting (Figure 4(c)).

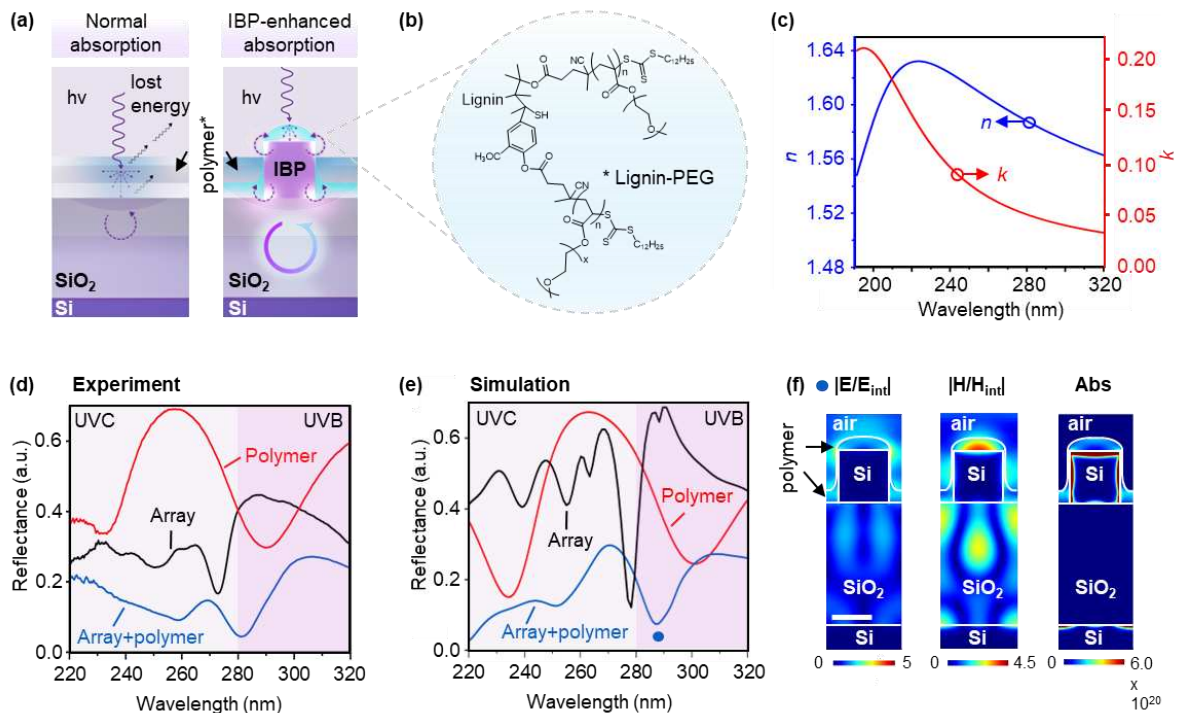


Figure 4. IBP-enhanced absorption of lignin-PEG polymer films within the UVB and UVC spectral region. (a) Illustration on the absorption of incident light by the lignin-PEG polymer film on the flat surface and on top of the Si nanodisk array. (b) Chemical structure of the lignin-PEG polymer. (c) Refractive index (n) and extinction coefficient (k) of the lignin-PEG film, obtained from ellipsometry measurements. (d)-(e) Experimental and simulated reflectance spectra of the Si array ($d = 130$ nm, $p = 200$ nm, $h_{SiO_2} = 300$ nm and $h_{Si} = 130$ nm), with and without a 55-nm-thick lignin-PEG polymer film, as well as the lignin-PEG reflectance on the flat substrate. (f) The spatial distribution of the electric field $|E/E_{int}|$ and magnetic field $|H/H_{int}|$ intensity, as well as the total power absorption distribution at the cross-section of the nanodisk with 55 nm lignin-PEG coating on top, at the wavelength of 287 nm. The scale bar denotes 100 nm.

In Figure 4(d), the experimental optical reflectance results are presented for the silicon nanodisk array with dimensions of $p = 200$ nm, $h_{Si} = 130$ nm and $d = 130$ nm, before and after depositing a 55-nm-thick lignin-PEG film. The observed redshift and broadening of the plasmon dip indicate a weak coupling between the plasmon mode of the array and the lignin-containing polymer. Primarily, the resonance band of the coupled system (*i.e.*, 55-nm lignin-PEG films on silicon plasmonic cavity) reaches near-zero reflectance, *i.e.*, $R = 0$. It implies a near perfect absorption, since $A = 100\% - R - T$, since the transmittance T is 0 for the substrate. Further experimental results of the reflectance of lignin-PEG coated arrays are demonstrated in Figure S11, showing the optical changes of Si nanodisk arrays of different diameters when coated with 55 nm and 70 nm lignin-PEG films.

To further analyze the reflectance/absorption characteristics of the polymer-coated arrays, FDTD simulations were performed based on the n and k values, as measured from ellipsometry. The simulation results of the reflectance spectra demonstrate good agreement

with the experimental data, as shown in Figure 4(e), with the corresponding spatial distributions of the electric field, magnetic field and absorption at the peak absorption wavelength of 278 nm are shown in Figure 4(f). In addition, Figure S12 presents the comparison of the absorption properties of the 55-nm lignin-PEG thin film on the flat substrate region and the one integrated with Si plasmonics. It shows that the hybrid polymer-silicon cavity has a 5.4-fold enhanced absorption as compared to the flat substrate case, at the peak absorption wavelength of 278 nm.

Therefore, by leveraging the hybridization of plasmonic and cavity modes, we demonstrate that the Q -factor of the plasmonic resonance can be significantly enhanced in order to offer similar benefits in the UV region as conventional plasmonic materials do in the visible region. In particular, the improved Q -factor of the IBP resonance can significantly enhance the absorption of a thin layer of UV-specific materials, which can prove useful in a number of optoelectronic applications relying on UV-active processes.^{40, 41} Preliminary results have also shown that in addition to tuning the optical response through cavity thickness and nanodisk geometry, another avenue for tunability lies in the introduction of symmetry breaking in the nanostructure design.^{42, 43} As demonstrated in our simulations in Figure S13, elliptical nanodisks with a tilted geometry exhibit distinct polarization-dependent optical responses, exhibiting a shift in the spectral positions of the hybridized resonance modes under different polarization states. This polarization-dependent response could potentially be leveraged for applications such as polarization-sensitive UV photodetectors and optical filtering devices.⁴⁴

45

Conclusions

Our study explores the design of IBP Si nanodisk and nanohole arrays with high Q -factor plasmon resonances within UVB and UVC spectral regions. The incorporation of a F - P -type SiO₂ cavity into the antenna design enables the hybridization between the LSPR

modes and the cavity modes. The Q -factor of the interband plasmon resonance can be significantly improved from ~ 1 to as high as 43 by variation of the cavity thickness. Using experimental measurements and FDTD simulations, we explored the absorption enhancement capabilities of Si arrays coated with a UV-absorbing lignin-PEG polymer. Our findings revealed that the hybrid polymer-silicon cavity has a 5.4-fold enhanced absorption as compared to the flat substrate with F - P cavity, at the peak absorption wavelength of 278 nm. These results highlight the potential of Si nanodisk arrays as IBP materials with high plasmon resonances with high Q -factors, which may pave the way towards enhanced performance in UV sensors, photodetectors and other optoelectronic devices.^{41, 46-48}

Author contributions.

E.C., Y.L., Z.D., and J.K.W.Y. conceived the concept, designed the experiments, wrote, and revised the manuscript. E.C. performed optical reflectance measurements. E.C., Y.L. and Q.R. performed the finite-difference time-domain (FDTD) simulations. D.K. and S.S. have synthesized and characterized the lignin-PEG polymer. Z.D. did the nanofabrication of the nanostructures. H.Y.L.L. performed Cr evaporation and SEM characterizations. S.D.R. performed the multipolar decomposition simulations. C.X. and A.R. did the ellipsometer characterization and analysis on the n and k values in the ultraviolet (UV) spectrum. F.T. did the dry etching of the samples. G.L. participated in discussions and provided insightful suggestions. All authors analyzed the data, read, and corrected the manuscript before the submission.

Supporting Information.

Additional details on simulation parameters, fabrication methods, and optical characterization.

Figures S1–S8: Simulated and experimental reflectance spectra, angle-resolved reflectance, and mode hybridization analysis. Figures S9–S12: Power absorption simulations and experimental reflectance data for lignin-PEG polymer coatings on arrays. Figure S13: Simulated reflectance and electric field distributions of an elliptical nanodisk array demonstrating polarization-dependent hybridized modes. The n and k values of the silicon material used for simulations is included as a text file. In addition, the methods of sample fabrication, synthesis process of lignin-PEG, optical characterization and modelling are included in supporting information.

Acknowledgements

Z.D. would like to acknowledge the funding support from the Agency for Science, Technology and Research (A*STAR) under its MTC IRG (Project No. M21K2c0116 and M22K2c0088), the Quantum Engineering Program 2.0 (Award No. NRF2021-QEP2-03-P09), DELTA-Q 2.0 (Project No. C230917005) and National Research Foundation (NRF) Singapore via Grant No. NRF-CRP30-2023-0003. J.K.W.Y. would like to acknowledge the funding support from National Research Funding (NRF) Singapore NRF-CRP20-2017-0001 and NRF-NRFI06-2020-0005.

References

- (1) Toudert, J.; Serna, R. Interband transitions in semi-metals, semiconductors, and topological insulators: a new driving force for plasmonics and nanophotonics [Invited]. *Opt. Mater. Express* **2017**, *7* (7), 2299-2325.
- (2) Toudert, J.; Serna, R. Ultraviolet-visible interband plasmonics with p-block elements. *Opt. Mater. Express* **2016**, *6* (7), 2434-2447.
- (3) Agarwal, A.; Vitiello, M. S.; Viti, L.; Cupolillo, A.; Politano, A. Plasmonics with two-dimensional semiconductors: from basic research to technological applications. *Nanoscale* **2018**, *10* (19), 8938-8946.
- (4) S. Zhang, S. A., M. Dai, Q. Y. S. Wu, N. Q. Adanan, J. Zhang, Y. Liu; et al Chalcogenide Metasurfaces Enabling Wideband Detectors from Visible to Mid-Infrared. *arXiv* **2024**.
- (5) Toudert, J.; Serna, R.; Camps, I.; Wojcik, J.; Mascher, P.; Rebollar, E.; Ezquerra, T. A. Unveiling the Far Infrared-to-Ultraviolet Optical Properties of Bismuth for Applications in

Plasmonics and Nanophotonics. *The Journal of Physical Chemistry C* **2017**, *121* (6), 3511-3521.

(6) McMahon, J. M.; Schatz, G. C.; Gray, S. K. Plasmonics in the ultraviolet with the poor metals Al, Ga, In, Sn, Tl, Pb, and Bi. *Physical Chemistry Chemical Physics* **2013**, *15* (15), 5415-5423.

(7) Camden, J. P.; Dieringer, J. A.; Zhao, J.; Van Duyne, R. P. Controlled Plasmonic Nanostructures for Surface-Enhanced Spectroscopy and Sensing. *Accounts of Chemical Research* **2008**, *41* (12), 1653-1661.

(8) Chowdhury, M. H.; Ray, K.; Gray, S. K.; Pond, J.; Lakowicz, J. R. Aluminum Nanoparticles as Substrates for Metal-Enhanced Fluorescence in the Ultraviolet for the Label-Free Detection of Biomolecules. *Analytical Chemistry* **2009**, *81* (4), 1397-1403.

(9) Jha, S. K.; Ahmed, Z.; Agio, M.; Ekinici, Y.; Löffler, J. F. Deep-UV Surface-Enhanced Resonance Raman Scattering of Adenine on Aluminum Nanoparticle Arrays. *Journal of the American Chemical Society* **2012**, *134* (4), 1966-1969.

(10) Heremans, J. P.; Cava, R. J.; Samarth, N. Tetradymites as thermoelectrics and topological insulators. *Nature Reviews Materials* **2017**, *2* (10), 17049.

(11) Poudel, B.; Hao, Q.; Ma, Y.; Lan, Y.; Minnich, A.; Yu, B.; Yan, X.; Wang, D.; Muto, A.; Vashaee, D.; et al. High-Thermoelectric Performance of Nanostructured Bismuth Antimony Telluride Bulk Alloys. *Science* **2008**, *320* (5876), 634-638.

(12) Tao, A.; Sinsersuksakul, P.; Yang, P. Tunable plasmonic lattices of silver nanocrystals. *Nature Nanotechnology* **2007**, *2* (7), 435-440.

(13) Todorov, R.; Hristova-Vasileva, T.; Katrova, V.; Atanasova, A. Silver and Gold Containing Compounds of p-Block Elements As Perspective Materials for UV Plasmonics. *ACS Omega* **2023**, *8* (16), 14321-14341.

(14) Piccinotti, D.; Gholipour, B.; Yao, J.; MacDonald, K. F.; Hayden, B. E.; Zheludev, N. I. Stoichiometric Engineering of Chalcogenide Semiconductor Alloys for Nanophotonic Applications. *Advanced Materials* **2019**, *31* (14), 1807083.

(15) Wredh, S.; Dai, M.; Hamada, K.; Rahman, M. A.; Adanan, N. Q.; Zamiri, G.; Wu, Q. Y. S.; Zhai, W.; Mun, N. W. L.; Dong, Z.; et al. Sb₂Te₃-Bi₂Te₃ Direct Photo-Thermoelectric Mid-Infrared Detection. *Advanced Optical Materials* **2024**, *12* (31), 2401450.

(16) Dong, Z.; Wang, T.; Chi, X.; Ho, J.; Tserkezis, C.; Yap, S. L. K.; Rusydi, A.; Tjiptoharsono, F.; Thian, D.; Mortensen, N. A.; et al. Ultraviolet Interband Plasmonics With Si Nanostructures. *Nano Letters* **2019**, *19* (11), 8040-8048.

(17) Li, M.; Cushing, S. K.; Wu, N. Plasmon-enhanced optical sensors: a review. *Analyst* **2015**, *140* (2), 386-406.

(18) Berini, P. Surface plasmon photodetectors and their applications. *Laser & Photonics Reviews* **2014**, *8* (2), 197-220.

(19) Lin, K.-T.; Lin, H.; Jia, B. Plasmonic nanostructures in photodetection, energy conversion and beyond. *Nanophotonics* **2020**, *9* (10), 3135-3163.

(20) Wang, B.; Yu, P.; Wang, W.; Zhang, X.; Kuo, H.-C.; Xu, H.; Wang, Z. M. High-Q Plasmonic Resonances: Fundamentals and Applications. *Advanced Optical Materials* **2021**, *9* (7), 2001520.

(21) Zhu, X.; Imran Hossain, G. M.; George, M.; Farhang, A.; Cicek, A.; Yanik, A. A. Beyond Noble Metals: High Q-Factor Aluminum Nanoplasmonics. *ACS Photonics* **2020**, *7* (2), 416-424.

(22) Chorsi, H. T.; Lee, Y.; Alù, A.; Zhang, J. X. J. Tunable plasmonic substrates with ultrahigh Q-factor resonances. *Scientific Reports* **2017**, *7* (1), 15985.

(23) West, P. R.; Ishii, S.; Naik, G. V.; Emani, N. K.; Shalaev, V. M.; Boltasseva, A. Searching for better plasmonic materials. *Laser & Photonics Reviews* **2010**, *4* (6), 795-808.

- (24) Artar, A.; Yanik, A. A.; Altug, H. Fabry–Pérot nanocavities in multilayered plasmonic crystals for enhanced biosensing. *Applied Physics Letters* **2009**, *95* (5).
- (25) Ameling, R.; Langguth, L.; Hentschel, M.; Mesch, M.; Braun, P. V.; Giessen, H. Cavity-enhanced localized plasmon resonance sensing. *Applied Physics Letters* **2010**, *97* (25).
- (26) Ciraci, C.; Hill, R. T.; Mock, J. J.; Urzhumov, Y.; Fernández-Domínguez, A. I.; Maier, S. A.; Pendry, J. B.; Chilkoti, A.; Smith, D. R. Probing the Ultimate Limits of Plasmonic Enhancement. *Science* **2012**, *337* (6098), 1072-1074.
- (27) Bahramipanah, M.; Dutta-Gupta, S.; Abasahl, B.; Martin, O. J. F. Cavity-Coupled Plasmonic Device with Enhanced Sensitivity and Figure-of-Merit. *ACS Nano* **2015**, *9* (7), 7621-7633.
- (28) Reinhard, B. M. Plasmonic Enhancement Strategies for Light-Driven Microbe Inactivation. *The Journal of Physical Chemistry C* **2022**, *126* (5), 2325-2335.
- (29) Kunz, J. N.; Voronine, D. V.; Lu, W.; Liege, Z.; Lee, H. W. H.; Zhang, Z.; Scully, M. O. Aluminum plasmonic nanoshielding in ultraviolet inactivation of bacteria. *Scientific Reports* **2017**, *7* (1), 9026.
- (30) Zhou, N.; López-Puente, V.; Wang, Q.; Polavarapu, L.; Pastoriza-Santos, I.; Xu, Q.-H. Plasmon-enhanced light harvesting: applications in enhanced photocatalysis, photodynamic therapy and photovoltaics. *RSC Advances* **2015**, *5* (37), 29076-29097.
- (31) An, C.; Wang, S.; Sun, Y.; Zhang, Q.; Zhang, J.; Wang, C.; Fang, J. Plasmonic silver incorporated silver halides for efficient photocatalysis. *Journal of Materials Chemistry A* **2016**, *4* (12), 4336-4352.
- (32) Anker, J. N.; Hall, W. P.; Lyandres, O.; Shah, N. C.; Zhao, J.; Van Duyne, R. P. Biosensing with plasmonic nanosensors. *Nature Materials* **2008**, *7* (6), 442-453.
- (33) Zhao, D.; Lin, Z.; Zhu, W.; Lezec, H. J.; Xu, T.; Agrawal, A.; Zhang, C.; Huang, K. Recent advances in ultraviolet nanophotonics: from plasmonics and metamaterials to metasurfaces. *Nanophotonics* **2021**, *10* (9), 2283-2308.
- (34) Qu, Y.; Bai, Y.; Aba, T.; Ullah, H.; Abudukelimu, A.; Huang, J.; Gou, T.; Li, J.; Zhang, Z. Chiral Near-Fields Induced by Plasmonic Chiral Conic Nanoshell Metallic Nanostructure for Sensitive Biomolecule Detection. *The Journal of Physical Chemistry C* **2020**, *124* (25), 13912-13919.
- (35) Ho, J.; Dong, Z.; Leong, H. S.; Zhang, J.; Tjiptoharsono, F.; Daqiqeh Rezaei, S.; Goh, K. C. H.; Wu, M.; Li, S.; Chee, J.; et al. Miniaturizing color-sensitive photodetectors via hybrid nanoantennas toward submicrometer dimensions. *Science Advances* **2022**, *8* (47), eadd3868.
- (36) Yang, Y.; Yoon, G.; Park, S.; Namgung, S. D.; Badloe, T.; Nam, K. T.; Rho, J. Revealing Structural Disorder in Hydrogenated Amorphous Silicon for a Low-Loss Photonic Platform at Visible Frequencies. *Advanced Materials* **2021**, *33* (9), 2005893.
- (37) Overvig, A. C.; Malek, S. C.; Carter, M. J.; Shrestha, S.; Yu, N. Selection rules for quasibound states in the continuum. *Physical Review B* **2020**, *102* (3), 035434.
- (38) Azzam, S. I.; Shalaev, V. M.; Boltasseva, A.; Kildishev, A. V. Formation of Bound States in the Continuum in Hybrid Plasmonic-Photonic Systems. *Physical Review Letters* **2018**, *121* (25), 253901.
- (39) Yew, P. Y. M.; Zhu, D. D.; Lin, Q. Y.; Jiang, L.; Chee, P. L.; Leong, H. S.; Dong, Z.; Guo, X. D.; Kai, D.; Loh, X. J. Synergistic UV protection effects of the lignin nanodiamond complex. *Materials Today Chemistry* **2021**, *22*, 100574.
- (40) Shao, D.; Zhu, W.; Liu, X.; Li, M.; Chen, J.; Sun, Y.-Y.; Xin, G.; Lian, J.; Sawyer, S. Ultrasensitive UV Photodetector Based on Interfacial Charge-Controlled Inorganic Perovskite–Polymer Hybrid Structure. *ACS Applied Materials & Interfaces* **2020**, *12* (38), 43106-43114.
- (41) Qiu, Q.; Huang, Z. Photodetectors of 2D Materials from Ultraviolet to Terahertz Waves. *Advanced Materials* **2021**, *33* (15), 2008126.

- (42) Dong, Z.; Jin, L.; Rezaei, S. D.; Wang, H.; Chen, Y.; Tjiptoharsono, F.; Ho, J.; Gorelik, S.; Ng, R. J. H.; Ruan, Q.; et al. Schrödinger's red pixel by quasi-bound-states-in-the-continuum. *Science Advances* **2022**, *8* (8), eabm4512.
- (43) Dong, Z.; Mahfoud, Z.; Paniagua-Domínguez, R.; Wang, H.; Fernández-Domínguez, A. I.; Gorelik, S.; Ha, S. T.; Tjiptoharsono, F.; Kuznetsov, A. I.; Bosman, M.; et al. Nanoscale mapping of optically inaccessible bound-states-in-the-continuum. *Light: Science & Applications* **2022**, *11* (1), 20.
- (44) Yan, L.; Li, Y.; Chandrasekar, V.; Mortimer, H.; Peltoniemi, J.; Lin, Y. General review of optical polarization remote sensing. *International Journal of Remote Sensing* **2020**, *41* (13), 4853-4864.
- (45) Shen, Z.; Lin, X. A review of metasurface polarization devices. *Optical Materials* **2023**, *146*, 114567.
- (46) Xia, Y.; Zhou, L.; Yang, J.; Du, P.; Xu, L.; Wang, J. Highly Sensitive and Fast Optoelectronic Room-Temperature NO₂ Gas Sensor Based on ZnO Nanorod-Assembled Macro-/Mesoporous Film. *ACS Applied Electronic Materials* **2020**, *2* (2), 580-589.
- (47) Razeghi, M.; Rogalski, A. Semiconductor ultraviolet detectors. *Journal of Applied Physics* **1996**, *79* (10), 7433-7473.
- (48) Huang, H.; Lai, J.; Lu, J.; Li, Z. Performance enhancement of ZnO ultraviolet detector by localized surface plasmon resonance of Al nanoparticles. *Applied Physics A* **2021**, *127* (9), 679.

Table of Content (TOC):

